JOURNAL OF AIRCRAFT
Vol. 52, No. 3, May–June 2015

Unsteady High-Angle-of-Attack Aerodynamic Models of a Generic Jet Transport

Dirk M. Luchtenburg*
The Cooper Union, New York, New York 10003
and
Clarence W. Rowley,† Mark W. Lohry,‡ Luigi Martinelli,§ and Robert F. Stengel¶
Princeton University, Princeton, New Jersey 08544

DOI: 10.2514/1.C032976

Accurate simulation of flight beyond normal conditions requires models of the aircraft aerodynamics at high angles of attack, for which the flow over the wing and control surfaces may be rapidly changing and massively separated. This study focuses on large-amplitude forced oscillations of a benchmark commercial aircraft configuration. Existing models are modified to describe the unsteady aerodynamic forces on the aircraft up to stall range. Steady-state and periodically forced unsteady Reynolds-averaged Navier–Stokes simulation data are employed to calibrate the model parameters. The results of the reduced-order models are in good overall agreement with those observed in the unsteady Reynolds-averaged Navier–Stokes simulations.

Nomenclature

AR	=	aspect ratio
a	=	speed of sound
c	=	chord length
c_D	=	drag coefficient
c_L	=	lift coefficient
c_M	=	pitching coefficient
c_l	=	section lift coefficient
f	=	forcing frequency
k	=	reduced frequency
Ma	=	Mach number
$\boldsymbol{R}(\boldsymbol{W})$	=	vector of the residuals
Re	=	Reynolds number
U_∞	=	incoming flow velocity
$\boldsymbol{W}$	=	vector of the flow variables
x	=	separation indicator
α	=	angle of attack
α_0	=	angle of attack at lift coefficient of zero
Δt	=	time step
ν	=	kinematic viscosity
ρ	=	density
$\tau_{1,2}$	=	relaxation times
Ω	=	angular actuation frequency

Received 2 May 2014; revision received 24 November 2014; accepted for publication 28 December 2014; published online 6 March 2015.

*Visiting Assistant Professor, Department of Mechanical Engineering, 41 Cooper Square; dluchten@cooper.edu.

†Professor, Department of Mechanical and Aerospace Engineering, School of Engineering and Applied Science; cwrowley@princeton.edu. Associate Fellow AIAA.

‡Ph.D. Candidate, Department of Mechanical and Aerospace Engineering, School of Engineering and Applied Science; mlohry@princeton.edu. Member AIAA.

§Associate Professor, Department of Mechanical and Aerospace Engineering, School of Engineering and Applied Science; gigi@phantom2.princeton.edu. Associate Fellow AIAA.

¶Professor, Department of Mechanical and Aerospace Engineering, School of Engineering and Applied Science; stengel@princeton.edu. Associate Fellow AIAA.

I. Introduction

HIGH-FIDELITY flight simulators currently used for training airline pilots portray flight dynamics within normal flight envelopes well, but they do not provide adequate preparation for flight with large angles of attack and sideslip, and high angular rates. Flight simulator models must be significantly improved to reduce the likelihood of future aircraft incidents and accidents. This requires the development of aerodynamic models that are valid not only for the normal flight envelope but also for the extended flight envelope, including stall and poststall conditions.

In this paper, we focus on aerodynamic models for longitudinal large-amplitude sinusoidal motions of a generic wide-body aircraft. In particular, we employ the so-called Common Research Model (CRM), which is a benchmark configuration for computational fluid dynamics (CFD) simulations and was developed by NASA and The Boeing Company [1]. We study two configurations: 1) a wing–body configuration, and 2) a more realistic configuration that includes horizontal and vertical stabilizers. The aerodynamic data are generated by CFD simulations of the unsteady Reynolds-averaged Navier–Stokes (URANS) equations. The objective is to obtain models that accurately capture the poststall effects described previously, especially for angles of attack up to 10 deg beyond the point of maximum C_L.

The aerodynamic models that we employ are motivated by the Goman–Khrabrov models for separated flow past a symmetric two-dimensional wing and a slender delta wing [2]. We modify the former model to account for finite nonsymmetric wings, and we identify its parameters such that a low-dimensional aerodynamic model is obtained for the lift coefficient of the CRM. We validate our aerodynamic models and find a good overall agreement with the CFD data. Thus, we show that the Goman–Khrabrov modeling approach works well for a complex commercial aircraft configuration with multiple lifting surfaces and three-dimensional unsteady separation.

II. Numerical Simulation

A. Common Research Model

We consider the flow over two different configurations of the so-called Common Research Model (see Fig. 1). This configuration is representative of wide-body commercial aircraft and was developed by NASA and The Boeing Company [1] as a benchmark for computational fluid dynamics predictions. In Fig. 1a, the wing–body configuration is shown; and in Fig. 1b, a more complete aircraft that includes horizontal and vertical stabilizers is shown. The former geometry is available for download from NASA and comes with a unified baseline grid for CFD [3]. The more complete aircraft is an extended version of the wing–body–horizontal-stabilizer CRM

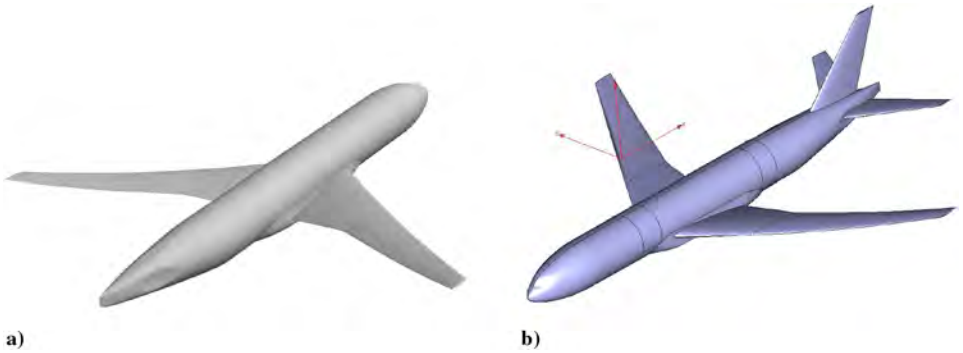

a) b)

Fig. 1 Common Research Model geometry: a) wing–body configuration, and b) wing–body–horizontal and vertical stabilizer configuration.

configuration. A simple vertical stabilizer was added, with the planform sizing and position chosen to mimic the Boeing 777. The airfoil transitions from a NACA 0010 at the root to a NACA 0008 at the tip. For details about the geometry and dimensions, we refer to [1]. In the following, all physical variables are assumed nondimensionalized with respect to the reference chord length c, the incoming flow velocity U_∞, and the constant density ρ. The flow is considered at the Reynolds number of $Re = U_\infty c/\nu = 3.26 \cdot 10^7$, where ν is the kinematic viscosity of the fluid, and at a Mach number of $Ma = U_\infty/a = 0.2$, where a is the speed of sound. The angle of attack of the aircraft configuration varies from 0 to 40 deg, with 0 deg defined by the longitudinal axis defined in [1].

Unsteady aerodynamic forces are introduced by sinusoidal variations of the angle of attack. The varying angle of attack is prescribed by

$$\alpha(t) = \hat{\alpha}(1 - \cos(\Omega t)) \tag{1}$$

where Ω is the angular actuation frequency, and $\hat{\alpha}$ determines the maximum angle of attack ($0 \text{ deg} \leq \alpha(t) \leq 2\hat{\alpha}$ deg. This frequency is given by $\Omega = 2k$, where

$$k = \pi f c/U_\infty \tag{2}$$

represents the reduced frequency with forcing frequency f.

B. Unsteady Reynolds-Averaged Navier–Stokes Simulation

The flow around the CRM configurations is modeled by the unsteady Reynolds-averaged Navier–Stokes equations. Small-scale turbulent fluctuations are incorporated by the two-equation shear stress transport k-ω turbulence model of Menter, which is noted to produce good results in separated flows [4,5]. The URANS equation is discretized by a compressible finite volume scheme of second-order accuracy in space and time.

The space discretization procedure is implemented separately from the discretization in time, leading to a set of coupled ordinary differential equations that can be written in the form

$$\frac{\mathrm{d}\boldsymbol{W}}{\mathrm{d}t} + \boldsymbol{R}(\boldsymbol{W}) = 0 \tag{3}$$

where $\boldsymbol{W}$ is the vector of the flow variables at the mesh locations, and $\boldsymbol{R}(\boldsymbol{W})$ is the vector of the residuals, consisting of the flux balances defined by the spatial discretization together with the added dissipative terms. For steady flow, such as those used for validation, multigrid acceleration is applied to an optimized multistage time-stepping scheme, which yields rapid convergence even for the large meshes used in this study.

A time-accurate simulation is achieved using the second-order backward difference formula [6,7]:

$$\frac{3}{2\Delta t}\boldsymbol{W}^{n+1} - \frac{2}{\Delta t}\boldsymbol{W}^{n} + \frac{1}{2\Delta t}\boldsymbol{W}^{n-1} + \boldsymbol{R}(\boldsymbol{W})^{n+1} = 0 \tag{4}$$

where $\boldsymbol{W}$, $\boldsymbol{R}$, Δt, and n are the conserved flow variables, solution residual, physical time-step size, and physical time iteration, respectively. This implicit scheme is A stable, allowing a choice of Δt based on the flow physics of interest. After a time-step refinement study, Δt was chosen corresponding to 1/10th of the convective time c/U_∞. This was seen to adequately resolve the effects of the poststall wake as well as the effects of the maneuvers.

The solution of implicit equation (4) is achieved by the use of a dual time-stepping approach:

$$\frac{\mathrm{d}\boldsymbol{W}}{\mathrm{d}t^*} + \frac{3}{2\Delta t}\boldsymbol{W} - \frac{2}{\Delta t}\boldsymbol{W}^{n} + \frac{1}{2\Delta t}\boldsymbol{W}^{n-1} + \boldsymbol{R}(\boldsymbol{W}) = 0 \tag{5}$$

where $t^\star$ is a pseudotime, which is advanced toward a steady state ($\boldsymbol{W} \to \boldsymbol{W}^{n+1}$) by using a full approximation storage multigrid time-stepping scheme, combined with local time stepping (in pseudotime), and residual averaging. This approach retains all the advantages of a fully implicit scheme with regard to time-step stability, whereas the explicit nature of the pseudotime stepping enables an efficient implementation on distributed multiprocessor systems using a message passing interface.

The numerical data used here have been obtained with the multiblock SUmb solver that was developed at Stanford University by van der Weide et al. [8]; and evolved from FLO107MB, originally developed at Princeton University by Martinelli et al. [9] and Reuther et al. [10].

The mesh used was a modification of the coarse, structured multiblock mesh provided for the 5th AIAA CFD Drag Prediction Workshop (DPW-V) [11]. The aft block of that mesh was removed and replaced by blocks, accommodating the new empennage using similar mesh spacing, resulting in a mesh of approximately 3 million cells, Computation was performed on a 128-core cluster consisting of eight 16-core AMD Opteron 6274 CPUs, requiring approximately 6 h of wall-clock time to compute four periods of a maneuver.

For validation purposes, we compute several points on the lift curve and drag polar at $Re = 5 \cdot 10^6$ and $Ma = 0.85$ for the CRM wing–body configuration, and we compare our results to those presented at a recent drag prediction workshop (DPW-V) [11]. Our computed lift curve presented in Fig. 2a is in excellent agreement with the "pseudotest" dataset, which was proposed in [11] as a correction of the experimental data obtained in the National Transonic Facility (NTF) at NASA Langley Research Center. In [11], it was argued that the wind-tunnel data deviate from the CFD data due to aeroelastic deformation of the model, which is confirmed by the agreement of the CFD results of a twisted-wing–body, which are also reported in Fig. 2a. Our computed drag polar in Fig. 2b is found to be in excellent agreement with the NTF experimental data. Thus, our computed results are well within the uncertainty range of all CFD results reported at the DPW-V, especially at higher angle of attacks $\Delta C_L < 0.05$, $\alpha = 4$ deg (the most relevant for the present study), even for a relatively coarse 3 million cell mesh. Based on this preliminary study, we are confident of the validity of our CFD analysis for the operating conditions considered in the rest of this paper (see Sec. II.A).

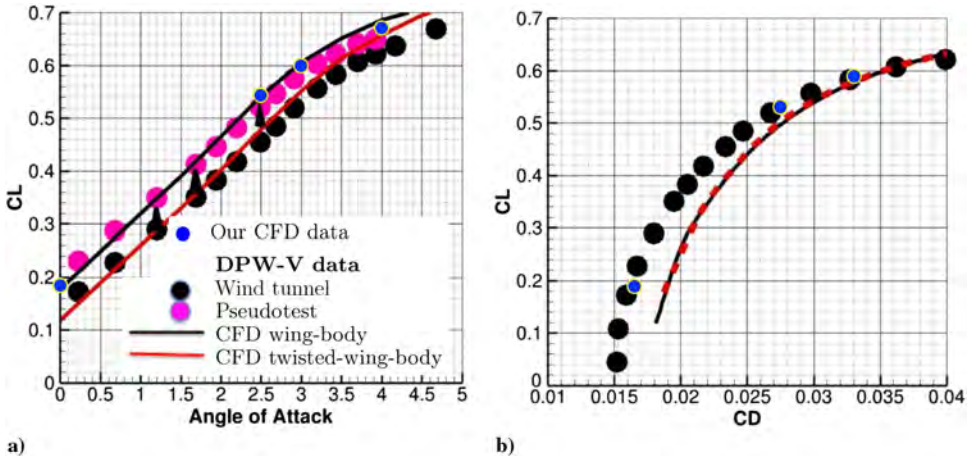

Fig. 2 Wing–body configuration: a) lift curve, and b) drag polar. Our CFD results are plotted on top of the NASA Langley results (see Sec. II.B).

III. Aerodynamic Modeling

A. Wing–Body Configuration

We start with a model for the lift coefficient of the wing–body configuration (see Fig. 1). The lift coefficient C_L increases with increasing angle of attack α and settles as the flow on the upper surface starts to separate at about $\alpha = 18$ deg (see Fig. 3). The flow separation begins at the trailing edge of the wing and moves to the leading edge as the angle of attack is increased. This form of flow separation is valid for relatively slow variations in angle of attack. For simplicity, we assume that the separation can be described by a single separation indicator x, where the value $x = 1$ corresponds to attached flow, whereas $x = 0$ corresponds to leading-edge flow separation. For a symmetric airfoil, the dependence of the section lift coefficient c_l on the angle of attack α and separation indicator x is given by [2]

$$c_l(\alpha, x) = 2\pi\alpha\left(\frac{1+\sqrt{x}}{2}\right)^2 \tag{6}$$

Note that, when the flow is fully attached ($x = 1$), the slope is 2π, which corresponds to the value for a two-dimensional thin airfoil. We modify the preceding expression to account for finite nonsymmetric wings. The slope 2π is replaced by the approximation

$$\frac{\mathrm{d}C_L}{\mathrm{d}\alpha} \approx \frac{2\pi AR}{(AR+2)} \tag{7}$$

for a finite wing with elliptical spanwise lift distribution [12], where AR is the aspect ratio of the wing ($AR > 8$). For the wing–body configuration, $AR = 9$; thus, $\mathrm{d}C_L/\mathrm{d}\alpha = 5.1$. The nonsymmetric contribution of the wing is incorporated by replacing α with $\alpha - \alpha_0$, where α_0 is the angle of attack corresponding to a lift coefficient of zero. Thus, we obtain the approximation

$$C_L(\alpha, x) = \frac{2\pi AR}{(AR+2)}(\alpha - \alpha_0)\left(\frac{1+\sqrt{x}}{2}\right)^2 \tag{8}$$

The static lift coefficient and its straight-line approximation are shown in Fig. 3a. The slope is approximately 4.8, which is slightly lower than the value given by Eq. (7). From the straight-line approximation, we also infer that $\alpha_0 = -2.3$ deg. In Fig. 3b, the dynamic lift coefficients for four large-amplitude forced oscillations at two different frequencies k [see Eq. (2)] are shown. As described in Sec. II.A, all forced oscillations are pure sinusoidal variations of the angle of attack; i.e., the pitch rate is zero. The angle of attack varies from 0 to 36 deg for maneuvers 1 and 2 (m1, m2), from 0 to 18 deg for maneuver 3 (m3), and from 0 to 28 deg for maneuver 4 (m4). For maneuvers 1, 2, and 3, the reduced frequency is $k = 0.010$; and for maneuver 2, it is $k = 0.021$. We assume that all lift coefficients can be (approximately) calculated by Eq. (8). Employing the values of α and C_L of the CFD data, we can solve Eq. (8) for x and obtain the corresponding separation indicator. The separation functions of the static data, and maneuvers 2 and 3 (compare with Fig. 3), are shown in Fig. 4. The results indicate that the flow fully separates at high angles of attack during maneuver 2 ($x \approx 0$), whereas for maneuver 3, the flow does not fully separate ($0.3 < x < 1$). Comparing the static separation function with the dynamic ones, we observe the effect of time delays associated with unsteady separation. This effect can be modeled by a first-order differential equation [2]:

$$\tau_1 \dot{x} + x = x_0(\alpha - \tau_2 \dot{\alpha}) \tag{9}$$

where x is the separation indicator for unsteady flow (see Fig. 4b), $x_0(\alpha)$ is the (quasi) stationary value of the separation point position for a given angle of attack (see Fig. 4a), and τ_i are relaxation times. Employing the identified static and dynamic separation functions,

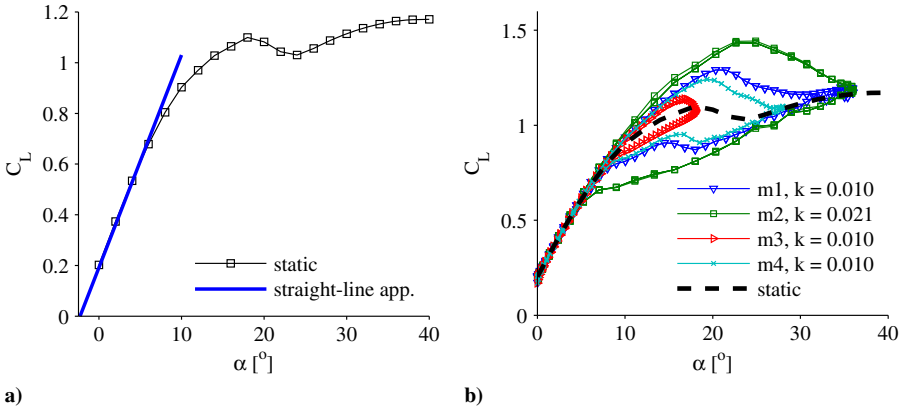

Fig. 3 Lift coefficient: a) static and straight-line approximation (app.), and b) dynamic lift coefficient for four maneuvers at two different frequencies k.

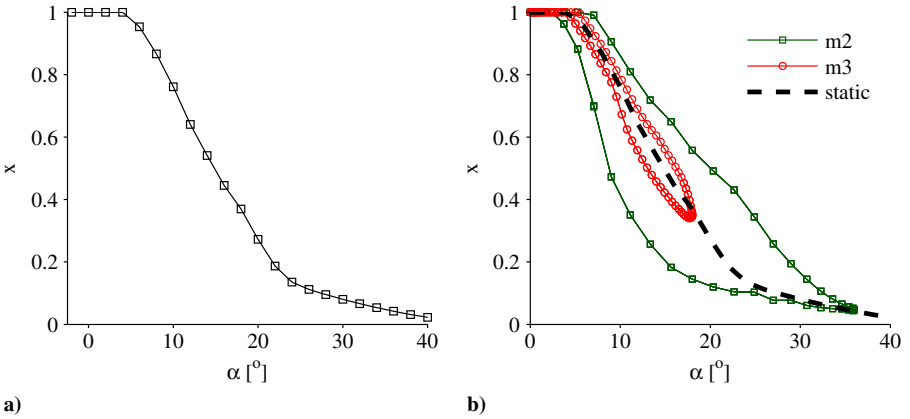

Fig. 4 Separation function: a) static, and b) dynamic for maneuvers 2 and 3.

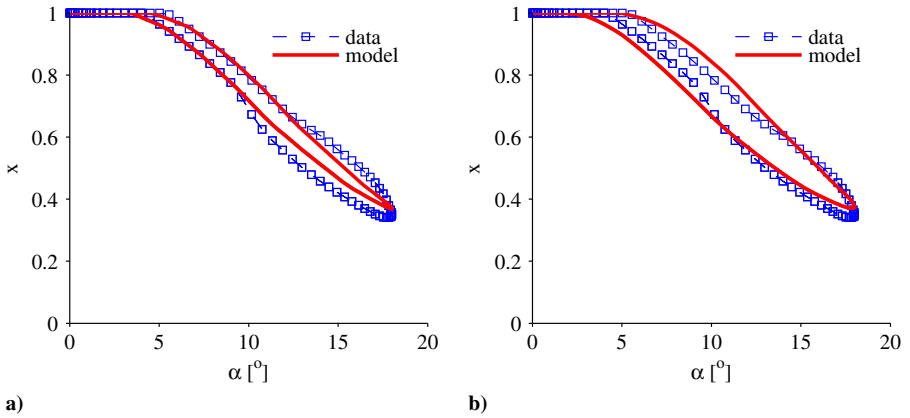

Fig. 5 Illustration of the calibration of relaxation times τ_1 and τ_2 using maneuver 3: a) step 1, and b) step 2.

the relaxation times are obtained by calibration. We calibrate as follows:

1) Set $\tau_1 = 0$ and adjust τ_2 such that all modeled envelopes of $x = x_0(\alpha - \tau_2\dot{\alpha})$ are within the envelopes of the fitted x of the CFD data, as shown in Fig. 4b. This step is shown for maneuver 3 in Fig. 5a.

2) Fix τ_2 and adjust τ_1 such that the modeled and fitted x of all maneuvers are reasonably close. This step is shown for maneuver 3 in Fig. 5b.

We find the following values for the relaxation times:

$$\tau_1 = 4.86\frac{c}{U_\infty}, \qquad \tau_2 = 3.89\frac{c}{U_\infty}$$

We emphasize that the calibrated values are the same for all maneuvers. Thus, we have obtained an unsteady aerodynamic model for the lift coefficient given by Eqs. (8) and (9). The lift coefficients of the CFD data and the model are shown in Fig. 6. The CFD data and model results are in fairly good agreement; most important, the trends of the CFD data are well captured by the simple aerodynamic model.

B. Wing–Body–Tail Configuration

In this section, we focus our attention on the wing–body–tail configuration, as shown in Fig. 1b. In Fig. 7, the static lift and pitching moment coefficients are shown. The slope of the straight-line approximation for the lift coefficient is $dC_L/d\alpha = 5.44$, which is slightly higher than the value given by Eq. (7); and zero lift is attained at $\alpha_0 = -1.8$ deg. We will use these values in the following. Both curves indicate that flow separation starts around $\alpha = 12$ deg. The pitching moment becomes more negative with an increasing angle of attack, which implies stable nosedown behavior. The plateau around $\alpha = 20$ deg is due to the relative position of the main wing and

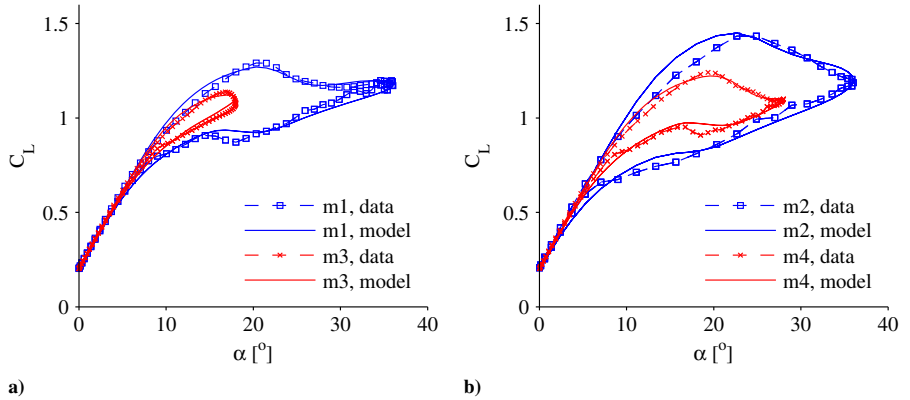

Fig. 6 Comparison of data and model lift coefficients: a) maneuvers 1 and 3, and b) maneuvers 2 and 4.

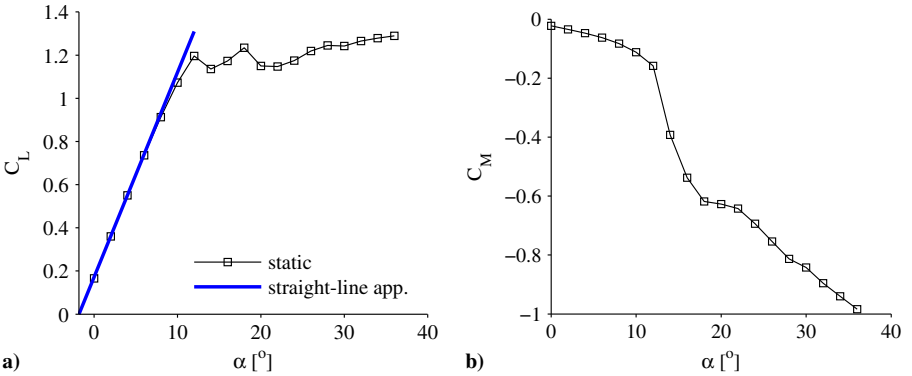

Fig. 7 Static curves for wing–body–tail configuration: a) lift, and b) pitching moment coefficient.

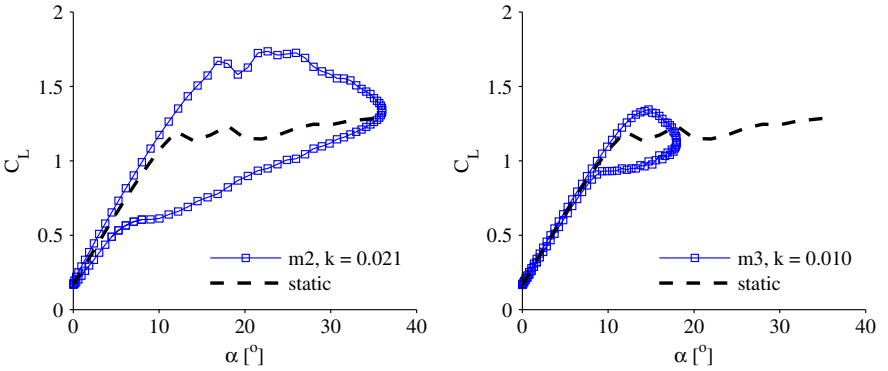

Fig. 8 Dynamic lift coefficient: a) maneuver 2, and b) maneuver 3 (compare with Fig. 3b).

horizontal stabilizer: at these angles of attack, the horizontal stabilizer is placed in the core section of the wake of the main wing. This "shadowing" of the horizontal stabilizer is also observed in the lift coefficient for dynamic maneuver 2, which dips around an angle of attack of 20 deg, as shown in Fig. 8a. This maneuver has the same frequency and amplitude as maneuver 2 for the wing–body configuration in Fig. 3b. During maneuver 3, the maximum angle of attack is less than 20 deg, and the influence of the wake on the horizontal stabilizer is negligible, as is clear from Fig. 8b.

As in Sec. III.A, we calibrate the model given by Eqs. (8) and (9) to fit the lift coefficients of the maneuvers that are shown in Fig. 8. First, we determine the static separation function; see Fig. 9a. Second, we determine all separation functions associated with the dynamic maneuvers. The separation functions for maneuvers 2 and 3 are shown in Fig. 9. These curves are not simple time delays of the static separation function, as was the case for the wing–body configuration (compare with Fig. 9). However, using the same calibration procedure as described previously in Sec. III.A, we determine the time constants such that the model best fits the CFD data. We find the following values:

$$\tau_1 = 7.77\frac{c}{U_\infty}, \qquad \tau_2 = 3.89\frac{c}{U_\infty}$$

A comparison between the model and CFD lift coefficients is shown in Fig. 10. The model predicts the overall trends, but it cannot capture the dip around $\alpha = 20$ deg during pitchup, where the horizontal stabilizer is affected by the wake of the main wing (the model only approximates time-shifted static behavior). In addition, the model fails to capture the undershoot at lower angles when the angle of attack is decreasing. The undershoot can be captured by including quadratic and cubic terms in Eq. (9).

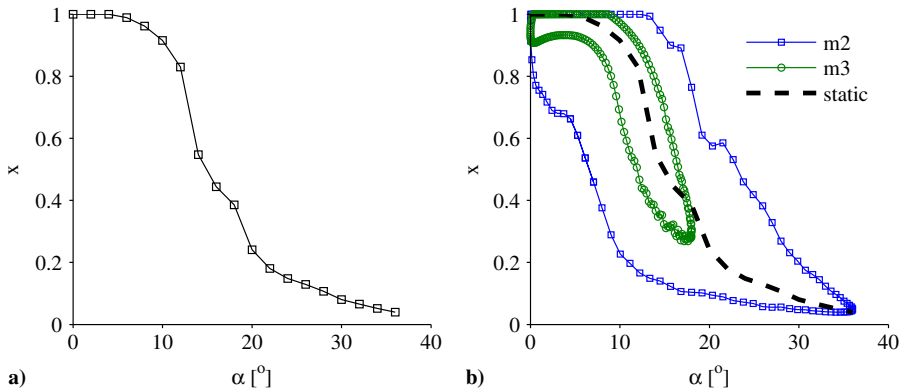

Fig. 9 Separation function: a) static, and b) maneuvers 2 and 3.

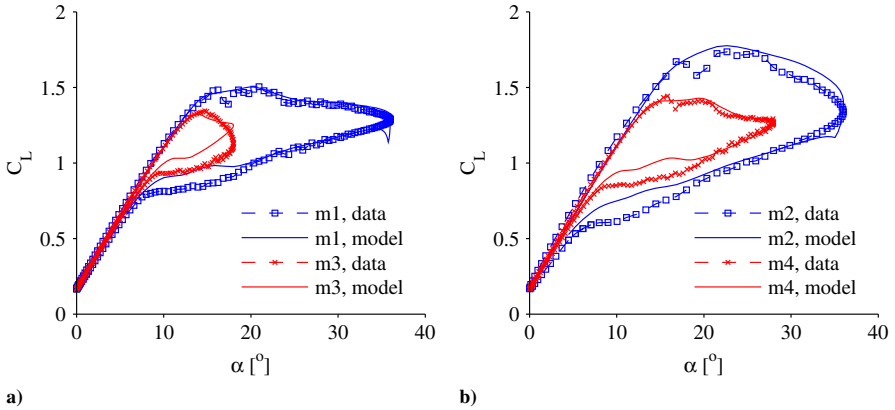

Fig. 10 Comparison of data and model lift coefficients: a) maneuvers 1 and 3, and b) maneuvers 2 and 4.

IV. Conclusions

A low-dimensional aerodynamic model was modified and calibrated for large-amplitude oscillations of two configurations of a generic wide-body aircraft: 1) a wing–body, and 2) a wing–body with horizontal and vertical stabilizer. This model provides a representation of the lift coefficient for normal, stall, and poststall longitudinal flight. The model is a modification of the model by Goman and Khrabrov [2], and it requires calibration of two parameters.

The model captures the URANS simulations surprisingly well, considering the very low order. The trends are in excellent agreement for the wing–body configuration, and the trends for the wing–body configuration with stabilizers is overall in good agreement. This agreement is important for realistic simulated flight. However, for the latter configuration, the effect of the main wing wake on the horizontal stabilizer is not modeled. In addition, the lift coefficient for the pitching-down motion is overpredicted. This can be expected, since all aerodynamic effects are lumped into a very low-order model, and a more accurate representation requires higher-order models.

A main advantage of the analytical model is the possibility of a simple and robust calibration of a given dataset. However, for even more realistic flight, including wake shadowing and other effects, a higher-order model might be required. Moreover, for stability purposes, it is important to have an aerodynamic model for the pitching moment coefficient. This will be a topic of future work.

Acknowledgment

This work was supported by the Federal Aviation Administration, award 12-G-008.

References

[1] Vassberg, J. C., DeHaan, M. A., Rivers, S. M., and Wahls, R. A., "Development of a Common Research Model," AIAA Paper 2008-6919, 2008.

[2] Goman, M. G., and Khrabrov, A. N., "State-Space Representation of Aerodynamic Characteristics of an Aircraft at High Angles of Attack," *Journal of Aircraft*, Vol. 31, No. 5, 1994, pp. 1109–1115. doi:10.2514/3.46618

[3] Vassberg, J. C., "A Unified Baseline Grid About the Common Research Model Wing-Body for the Fifth AIAA CFD Drag Prediction Workshop," AIAA Paper 2011-3508, 2011.

[4] Menter, F. R., "Two-Equation Eddy-Viscosity Turbulence Models for Engineering Applications," *AIAA Journal*, Vol. 32, No. 8, 1994, pp. 1598–1605. doi:10.2514/3.12149

[5] Martinelli, L., and Jameson, A., "Computational Aerodynamics: Solvers and Shape Optimization," *Journal of Heat Transfer*, Vol. 135, No. 1, 2012, Paper 011002. doi:10.1115/1.4007649

[6] Alonso, J., Martinelli, L., and Jameson, A., "Multigrid Unsteady Navier–Stokes Calculations with Aeroelastic Applications," AIAA Paper 1995-0048, 1995.

[7] Jameson, A., and Martinelli, L., "Mesh Refinement and Modeling Errors in Flow Simulation," *AIAA Journal*, Vol. 36, No. 5, 1998, pp. 676–686. doi:10.2514/2.453

[8] van der Weide, E., Kalitzin, G., Schluter, J., and Alonso, J., *Unsteady Turbomachinery Computations Using Massively Parallel Platforms*, AIAA Paper 2006-421, 2006.

[9] Martinelli, L., Alonso, J. J., Jameson, A., and Reuther, J., "CFD Analysis and Design Optimization Using Parallel Computers," *Some New Directions in Science on Computers*, edited by Bhanot, G., Chen, S., and Seiden, P., World Scientific, Singapore, ROS, 1997, pp. 3–40.

[10] Reuther, J., Alonso, J., Vassberg, J., Jameson, A., and Martinelli, L., "An Efficient Multiblock Method for Aerodynamic Analysis and Design on Distributed Memory Systems," AIAA Paper 1997-1893, 1997.

[11] Levy, D. W., Laflin, K. R., Tinoco, E. N., Vassberg, J. C., Mani, M., Rider, B., Rumsey, C., Wahls, R. A., Morrison, J. H., Brodersen, O. P., Crippa, S., Mavriplis, D. J., and Murayama, M., "Summary of Data from the Fifth AIAA CFD Drag Prediction Workshop," AIAA Paper 2013-0046, 2013.

[12] Stengel, R. F., *Flight Dynamics*, Princeton Univ. Press, Princeton, NJ, 2004, p. 71 (Eq. 2.4-7).